nature communications

Article

https://doi.org/10.1038/s41467-025-63843-y

Topological Luttinger-semimetal $CoAs_3$ dye-sensitized photocatalyst for efficient solar hydrogen evolution

Received: 21 February 2025

Accepted: 1 September 2025

Published online: 01 October 2025

Check for updates

Yuan Cao[1,7], Zhuo Han[2,7], Rui Song[3,7], Yuqi Liu[2], Shucai Xia[4], Xinlei Zhang[4], Jing Leng[4], Changhao Wang[2], Wenliang Zhu[1] ✉, Yin Yu[5], Xiaomin Tian[1], Jiaqi He[1], Yu Zou[1], Yi Ma[2] ✉, Jianzhi Gao[1] ✉, Chuanyao Zhou[4] ✉, Feng Song[6] ✉, Wei Huang[6] ✉ & Minghu Pan[1] ✉

Solar-driven photocatalytic water splitting is a process for hydrogen production from a renewable source. The practical implementation of this technology is limited by the low conversion efficiency of the hydrogen evolution reaction under visible light and the insufficient long-term stability of photocatalysts. Here we demonstrate a dye (Eosin Y)-sensitized photocatalyst for efficient hydrogen production. The topological semimetal $CoAs_3$ achieves a hydrogen production rate of 2688 μmol h^{-1} g^{-1} ($\lambda \geq 420$ nm) and an apparent quantum efficiency of 15.2% at $\lambda = 500$ nm. Efficient photocatalytic activity is attributed to the electronic properties of $CoAs_3$, which facilitate electron transfer at the Eosin Y/$CoAs_3$ interface, determined by transient absorption spectroscopy. Density functional theory calculations predict that $CoAs_3$ is a Luttinger semimetal, exhibiting a quadratic band touching point near the Fermi level and an associated topological insulator gap. The carrier mobility of the material facilitates the transfer of injected electrons from the dye to active sites. Herein, we report a topological photocatalyst that exhibits enhanced stability and efficiency for solar hydrogen production.

The amount of solar energy incident on the Earth in a single hour exceeds the total annual energy consumption of the global population. Consequently, solar energy represents a viable alternative to fossil fuels[1,2]. In order to facilitate the wider implementation of solar energy, it is essential to develop a framework for the sustainable and environmentally friendly storage of chemical fuels. Hydrogen is a candidate renewable fuel; it is an energy-dense carrier that produces only water upon combustion with oxygen[3–6].

The electrocatalytic hydrogen evolution reaction (HER) requires an external electrical input, the sustainability of which depends on its primary generation source. On the other hand, dye-sensitized photocatalysis (DSP) has been proven to be a promising method for directly converting solar energy into H_2 without using electric power. In our specific system for photocatalytic HER, tetrabromofluorescein (EY) is employed as the photosensitizer to absorb visible light[7,8]. For a standard DSP process, photoexcitation of the sensitizer is followed by electron–hole separation and transfer to the catalysts and sacrificial agents to initiate reductive and oxidative reactions, respectively[9,10]. The charge separation and transfer, which are crucial for the performance of DSP systems,

[1]School of Physics and Information Technology, Shaanxi Normal University, Xi'an, China. [2]School of Chemistry and Chemical Engineering, Shaanxi Normal University, Xi'an, China. [3]Science and Technology on Surface Physics and Chemistry Laboratory, Mianyang, PR China. [4]State Key Laboratory of Molecular Reaction Dynamics, Dalian Institute of Chemical Physics, Chinese Academy of Sciences, Dalian, China. [5]School of Precision Instrument and Opto-Electronics Engineering, Tianjin University, Tianjin, China. [6]School of Physics, Nankai University, Tianjin, China. [7]These authors contributed equally: Yuan Cao, Zhuo Han, Rui Song. ✉e-mail: wlzhu@snnu.edu.cn; mayi@snnu.edu.cn; jianzhigao@snnu.edu.cn; chuanyaozhou@dicp.ac.cn; fsong@nankai.edu.cn; weihuang@njtech.edu.cn; minghupan@snnu.edu.cn

require suitable catalysts with fast charge transfer kinetics, both internally and interfacially[11–15].

Until now, noble metals (and noble-metal-containing materials), such as Pt, Ir, and Pd, as well as the state-of-the-art HER catalysts showing high electrocatalytic HER performance[16–20], have been well studied, and some well-known concepts such as *d*-band theory have been proposed[21–25]. While noble metals exhibit favorable electron conductivity, their scarcity and cost limit large-scale application[26–28]. Consequently, a central challenge is the development of non-noble metal catalysts that exhibit comparable activity. Various low-cost catalysts based on earth-abundant materials have been explored for HER, such as transition metal chalcogenides[29,30], transition metal phosphides[31,32], transition metal carbides[33,34], transition metal nitrides[35,36], and so on. Non-noble metal photocatalysts with high carrier mobility and density are worth investigating for photocatalytic hydrogen production under visible light.

The possibilities for developing high-performance catalysts have been expanded after the discovery of topological materials[37,38]. Topological materials, which include topological insulators (TIs), topological semimetals (e.g., Dirac, Weyl, and nodal-line semimetals), and topological superconductors, are characterized by electronic boundary states protected by their band topology[39]. The protected surface states in topological materials host mobile charge carriers, a property expected to promote efficient charge transport and long-term stability, ultimately enhancing photocatalytic activity[37–40]. Several topological semimetals like (Nb,Ta)/(As,P) and MIrTe$_4$ (M = Nb,Ta) have been investigated for dye-sensitized HER, and the hydrogen production rate of NbIrTe$_4$ was reported to be 18,000 μmol g^{-1} (10 h)$^{-1}$[41]. However, the range of topological materials applied to photocatalytic systems is still limited. Moreover, the relationship between topological properties and the photocatalytic HER reaction process requires further investigation[41,42]. Further progress in photocatalytic HER is limited by two key challenges: inefficient utilization of solar light and the recombination of charge carriers. These challenges often cause low solar-to-hydrogen conversion efficiency and necessitate the exploration of photocatalysis with earth-abundant elements.

Our work aims to design an effective photocatalyst by exploring the properties of topological materials. The transition metal pnictide $CoAs_3$ is one of the promising candidates, as its predicted topological electronic structure is expected to yield favorable charge transport properties. In this work, we prepared the topological semimetal $CoAs_3$ for dye-sensitized HER, as well as other topological materials, including the semimetals WTe_2, HfP_2, and the insulators Mo_2C, Bi_2Te_3, and Bi_2Se_3. We evaluated the photocatalytic activity of these materials, found that the noble-metal-free photocatalyst $CoAs_3$ achieves a hydrogen production rate of 2688 μmol h^{-1} g^{-1} under visible light irradiation ($\lambda \geq 420$ nm). Furthermore, transient absorption (TA) spectroscopy and density functional theory (DFT) calculations indicate that this high catalytic activity can be attributed to effective electron transfer at the dye/$CoAs_3$ interface and the material's topological semimetal nature. Our results suggest that the carrier dynamics in such materials can be utilized to address the existing challenges, providing a foundation for designing improved photocatalysts.

Results and discussion

Characterizations of $CoAs_3$ compounds

The cubic crystalline structure of the skutterudite-type compounds $CoAs_3$ in the $Im\bar{3}$ symmetry is shown in the insert image in Fig. 1a, where the Co (deep blue) and As (green) atoms occupy the *8c* and *24g* Wyckoff positions, respectively. The six-coordinated octahedron is formed by one cobalt atom and six arsenic atoms, with a Co-As bond length of 2.345 Å. The powder X-ray diffraction (XRD) pattern (Fig. 1a) shows sharp diffraction peaks, all of which can be indexed to the cubic skutterudite phase, indicating a high crystalline quality and phase-pure sample. The diffraction patterns were indexed to the cubic space group $Im\bar{3}$ (Fig. 1a and Table s2). Rietveld refinement of the XRD data for $CoAs_3$ yielded lattice parameters consistent with previously reported values[43]. Scanning electron microscopy images (Fig. S13) show that the $CoAs_3$ crystals have an average size of 1.2 μm, with individual crystals ranging from 0.5 to 3 μm. Energy dispersive X-ray (EDX) spectroscopy mapping of a $CoAs_3$ microparticle (Fig. 1c–e) reveals a spatially uniform distribution of Co and As, with no other elements detected. The atomic structure of the $CoAs_3$ microcrystals was further investigated using high-resolution scanning transmission electron microscopy (HR-STEM) and selected-area electron diffraction (SAED). The HR-STEM images (Fig. 1h, i) and SAED pattern (Fig. 1g) confirm the crystal structure, and the measured lattice constants are consistent with reported values[44]. X-ray photoelectron spectroscopy (XPS) was used to analyze the chemical states of the $CoAs_3$ polycrystals (Fig. 1j, k). The Co 2*p* spectrum shows two main peaks at 779.3 eV ($2p_{3/2}$) and 794.3 eV ($2p_{1/2}$), which correspond to a mixed valence state of Co^{2+} and Co^{3+}. The As 3*d* spectrum exhibits peaks at 42.2 and 41.4 eV, corresponding to Co-As bonds. These binding energies are all consistent with previously reported values[45,46].

Photocatalytic activity of $CoAs_3$

To identify the topological properties beneficial for photocatalytic HER, we compared the dye-sensitized HER performance of $CoAs_3$ with that of other topological materials, including WTe_2, HfP_2, Mo_2C, Bi_2Te_3, and Bi_2Se_3. These materials were selected to represent a range of topological properties and band structures near the Fermi level (E_F) and were tested under identical experimental conditions. EY and triethanolamine (TEOA) were used as the photosensitizer and the sacrificial electron donor, respectively. The photocatalytic activity of these materials remains stable over 5 h (Fig. 2a); such stability may be attributed to their protected topological surface states[47,48]. Among these materials, $CoAs_3$ achieves a photocatalytic HER rate of 684 μmol h^{-1} g^{-1}, 14.3 times that of Bi_2Se_3. The electrochemically active surface area (ECSA) of each photocatalyst was determined from cyclic voltammetry measurements (Supplementary Figs. S1–S3). Although the ECSA of $CoAs_3$ (1.61×10^{-4} mF cm^{-2}) is approximately half that of Mo_2C, its photocatalytic activity exceeds that of other materials tested. This discrepancy points to the contribution of the electronic property of $CoAs_3$ to its catalytic activity, which we investigate in the following sections.

The photocatalytic activity of $CoAs_3$ was investigated by varying the catalyst mass and photosensitizer concentration. To determine the effect of catalyst mass, the concentrations of the EY and the TEOA were kept constant at 10 mg and 15 mL, respectively. Figure S4 shows that H_2 can be produced in the absence of $CoAs_3$ catalysts, and the activity increased with the addition of $CoAs_3$. Therefore, the hydrogen evolution rate attributed to $CoAs_3$ can be calculated by subtracting the rate of the control experiment from the total measured rate. As shown in Fig. 2b, the normalized activity of $CoAs_3$ remains stable between 1 and 25 mg, which well reflects the intrinsic activity of $CoAs_3$. When the catalyst mass was increased beyond 30 mg, the hydrogen evolution rate decreased. This rate decrease is attributed to the large amount of catalyst masking the active sites and blocking the light absorption[49]. Therefore, in subsequent experiments, the amount of $CoAs_3$ was fixed at 25 mg.

The dosage of photosensitizer was then adjusted from 10 to 80 mg, while keeping the catalyst and sacrificial agent constant (Fig. 2c). The hydrogen evolution rate initially increased as the amount of photosensitizer was raised. The rate reached a maximum value of 2697 μmol h^{-1}g^{-1} at a photosensitizer amount of 70 mg, and subsequently decreased when the amount was increased to 80 mg (Fig. 2c). This decrease at higher concentrations is attributed to two factors: (1) a shading effect caused by excess photosensitizer, and (2) collisional quenching of the excited photosensitizer (*EY) by ground-state EY

https://doi.org/10.1038/s41467-025-63843-y

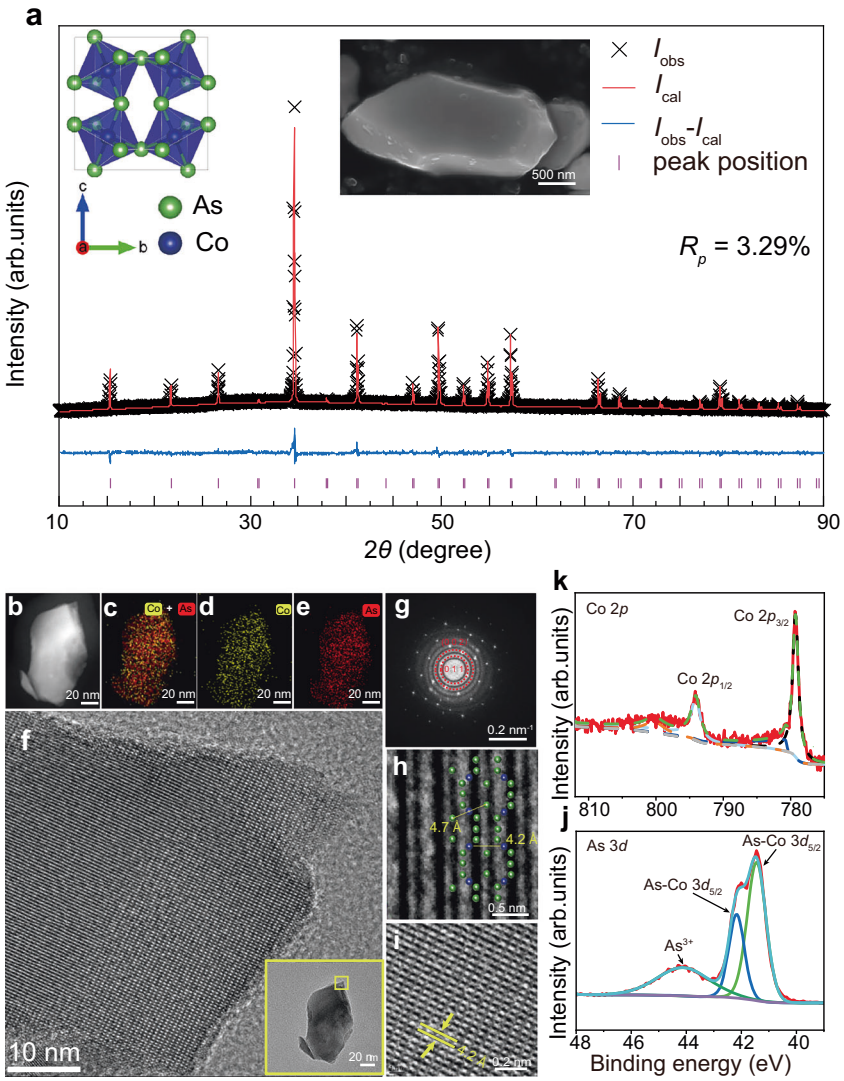

Fig. 1 | Crystalline structure, X-ray diffraction, SEM images, element mappings, and XPS characterization of $CoAs_3$ microcrystal. a The final Rietveld refinement of XRD spectrum of $CoAs_3$ polycrystals. (left insert) Structural model of $CoAs_3$ (space group $Im\bar{3}$). Blue and green balls represent Co and As atoms, respectively. (right insert) SEM image of $CoAs_3$ microcrystal. **b**–**e** SEM images (**b**) and element mappings of $CoAs_3$ flake, showing a uniform distribution of Co + As (**c**), Co (**d**), and As (**e**) elements. The average Co:As atomic ratio determined by the energy-dispersive X-ray spectroscopy (EDX) spectra is close to 1:3, and no foreign elements were detected within the detection limit of the instrument; **f**–**i** Atomic-level TEM image and low-magnification scanning transmission electron microscopy (STEM) image. (insert) of $CoAs_3$ microcrystals. The yellow rectangle at the top right of the insert graph indicates the area where the atomic-level TEM (**f**) and the selected-area electron diffraction (SAED) pattern (**g**) were measured. Red circles in (**g**) mark the primary diffraction spots. **h**, **i** Atomic-level TEM images of a $CoAs_3$ crystal taken at different locations, where 4.2 Å corresponds to the distance to the nearest neighboring Co. **j**, **k** X-ray photoemission spectroscopy (XPS) spectra of **j** Co 2*p* and **k** As 3*d* for freshly prepared $CoAs_3$ polycrystals. Source data for Fig. 1 are provided as a Source data file.

molecules, which can deactivate *EY before interfacial electron transfer occurs[11,50,51].

Control experiments show that hydrogen evolution is negligible in the absence of any of the three components: the $CoAs_3$ catalyst, the EY photosensitizer, or the TEOA sacrificial agent (Fig. 2d). Under full-spectrum irradiation, the hydrogen evolution rate increased to 3232 μmol $h^{-1}g^{-1}$. In contrast, graphene with super electron transfer efficiency was also used for comparison, which exhibits a lower activity compared with $CoAs_3$. These results suggest that $CoAs_3$ not only serves as an effective charge transfer material but also provides abundant HER active sites in this system. It is important to note that the rate of photocatalysis is likely to vary substantially depending on the effects of a given temperature, pressure, light intensity, and other factors. The ultraviolet–visible absorption spectra of $CoAs_3$ and Bi_2Se_3 exhibit minimal absorption in the visible range (Fig. S12). This property suggests they do not function as the primary light absorbers in this photosensitized system. The absorption peaks of pure EY solution are at 480 and 518 nm due to π-π* excitation[41], which is consistent with previous results[52]. When EY powder is mixed with $CoAs_3$ and Bi_2Se_3 powders, respectively, absorption peaks of 487 and 526 nm appear near the characteristic peaks of the dye, indicating a redshift. This redshift suggests an electronic interaction between EY and the $CoAs_3$ or Bi_2Se_3 materials. Such an interaction may facilitate the transfer of photogenerated electrons from the excited photosensitizer to the catalyst[53]. Additionally, a color change in the solution from red–orange to saffron was observed during the photocatalytic process, suggesting degradation of the EY photosensitizer over the reaction time.

The apparent quantum efficiency (AQE) was measured at several incident light wavelengths (Fig. 2e) (See the "Methods" section for detailed experimental and calculation procedures.). The $CoAs_3$-EY system exhibited a maximum AQE of 15.2% at an incident wavelength of 500 nm. Relatively high AQE values can also be obtained at 450 and

https://doi.org/10.1038/s41467-025-63843-y

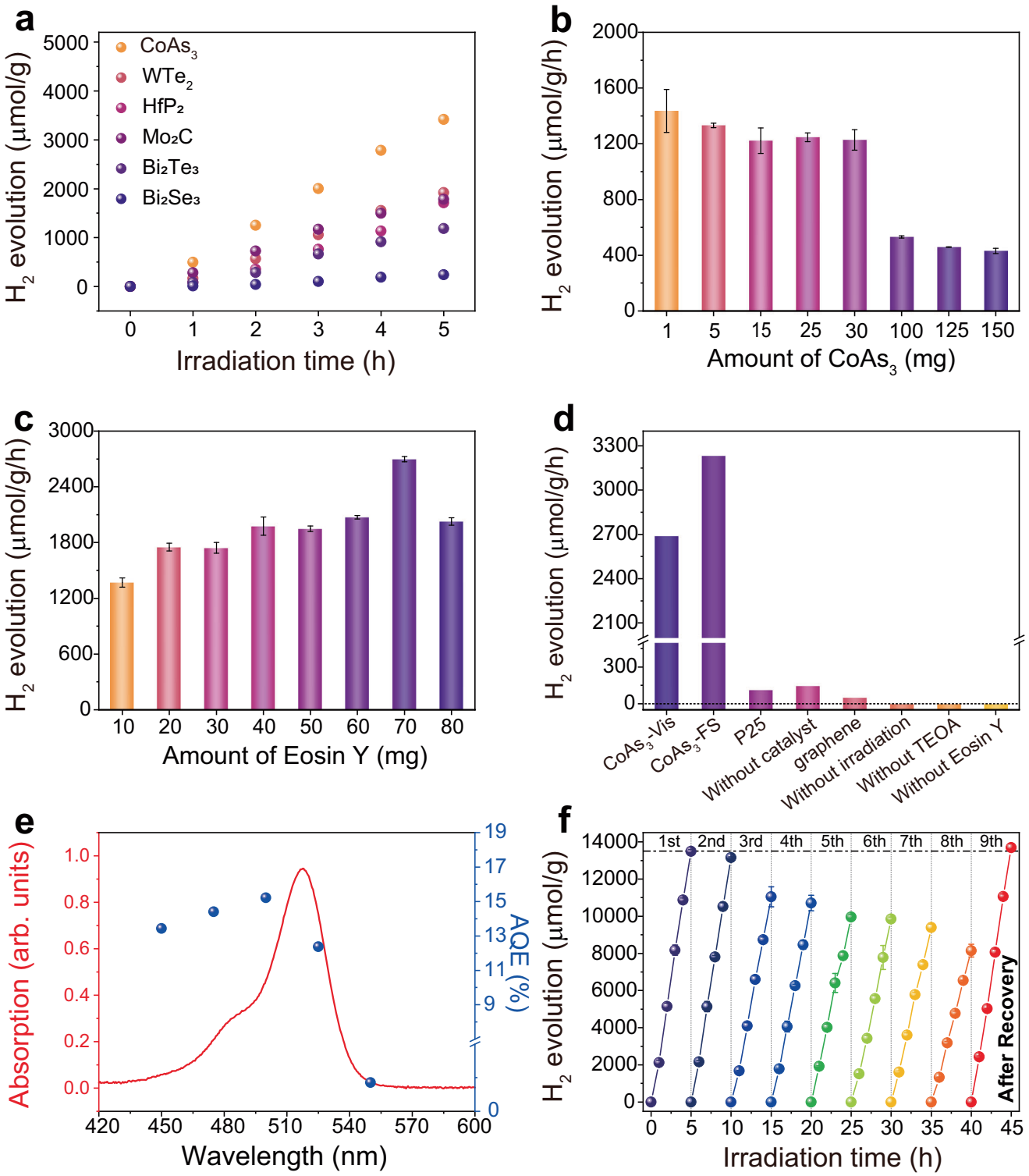

Fig. 2 | Photocatalytic activity of various topological materials. a Hydrogen production rates of $CoAs_3$, WTe_2, HfP_2, Mo_2C, Bi_2Te_3 and Bi_2Se_3. **b** Eosin Y dye-sensitized photocatalytic HER activity of $CoAs_3$ after 5 h of irradiation, normalized with respect to the catalyst amount in grams, with different amounts of catalyst. **c** Hydrogen production rate of $CoAs_3$ at different amounts of dye. **d** Control experiments of hydrogen production in the dye sensitization system. P25 represents for TiO_2 nanoparticles photocatalyst of ca. 25 nm. $CoAs_3$-Vis represents photocatalysis under visible light, while $CoAs_3$-FS refers to photocatalysis under a full-spectrum light. **e** The variation of the quantum apparent efficiency (AQE) of photocatalyst $CoAs_3$ vs. radiation wavelength (blue dots) and the UV-vis absorption spectrum of EY (red curve). **f** The reproducibility of the EY dye-sensitized photocatalytic hydrogen evolution reaction (HER) activity of $CoAs_3$ for the optimum dye/catalyst ratio. In (**b**, **c**, **f**), data are presented as mean ± s.d. from three independent experiments ($n = 3$). Source data for Fig. 2 are provided as a Source data file.

480 nm with lower EY absorption intensity. The system remains active at shorter wavelengths despite the reduced light absorption by the photosensitizer.

To investigate the stability of the $CoAs_3$ photocatalyst at the optimal ratio of 25 mg $CoAs_3$ and 70 mg photosensitizer, a set of cycling experiments with a unit cycle of 5 h was conducted. Over eight consecutive 5-h cycles, the hydrogen evolution rate showed a minor decrease in each cycle (Fig. 2f). In the recovery experiment (ninth cycle), the catalysts were cleaned and centrifuged before being reused in a fresh experimental solution. Upon reuse, the catalyst's activity was restored to its initial level, yielding 13,692 μmol g^{-1} of H_2 in 5 h. Due to the inferior stability of EY[54], the decreased activity of the DSP system may be ascribed to the reduced concentration of EY. Therefore, after the recovery of EY concentration, the activity can be well-restored, indicating a stable performance of $CoAs_3$ catalyst. The EDX and XPS analyses (Supplementary Fig. S5) of the catalysts performed after the cycling experiments showed no observable changes in their components or morphology. Collectively, these findings indicate that $CoAs_3$ is a structurally and functionally stable catalyst for photocatalytic hydrogen evolution.

Electron transfer efficiency at the EY/$CoAs_3$ interface

To investigate the electron-transfer process during DSP photocatalytic HER, amperometric current density *I*–*t* curves were measured (Supplementary Fig. S6) in a 0.1 M Na_2SO_4 and TEOA aqueous solution. In the absence of a catalyst, the EY-sensitized electrode exhibited a transient anodic photocurrent spike upon illumination. This feature is characteristic of charge accumulation at the electrode-sensitizer interface followed by rapid recombination, as the photogenerated electrons are not transferred to an acceptor[55–57]. This behavior indicates fast charge recombination when no effective electron acceptor presents[58,59].

In contrast, the introduction of $CoAs_3$ catalyst changes the carrier dynamics. For the EY/$CoAs_3$ system, the photocurrent increases throughout the illumination period. This photoactivation is attributed to light-induced effects that occurred at the dye-catalyst interface, such as a stable dye adsorption and a dynamic adsorption–desorption equilibrium, which enhance photosensitization efficiency[60]. Furthermore, the slow current decay after illumination ceases indicates that $CoAs_3$ possesses charge-storage capacity, allowing trapped electrons to subsequently participate in the HER[58]. Notably, while the EY/Bi_2Se_3 system shows a similar photoactivation trend, its total photocurrent density is much lower. This lower photocurrent is observed despite Bi_2Se_3 being a TI with surface states reported to support efficient charge transport. Therefore, this result strongly suggests that the rate-determining step is not charge transport but the slow kinetics of the surface HER. These comparative results indicate that the overall photoelectrochemical efficiency depends on a combination of interfacial charge separation, bulk transport, and surface reaction kinetics. The high performance of the EY/ $CoAs_3$ system should be due to a better balance of many factors, particularly the higher intrinsic HER activity and favorable photoactivation properties of the $CoAs_3$ surface.

The kinetics of interfacial charge transfer were investigated using electrochemical impedance spectroscopy. The charge transfer resistance (R_{ct}) of the EY-sensitized $CoAs_3$ and Bi_2Se_3 systems was compared. Both the EY/$CoAs_3$ and EY/Bi_2Se_3 systems exhibited their lowest R_{ct} at 520 nm, as shown in Fig. S11. This wavelength corresponds to the primary absorption peak of the EY photosensitizer, suggesting that the rate of electron injection from the excited dye to the catalyst is dependent on the amount of light absorbed. Moreover, under all comparable illumination wavelengths, the EY/$CoAs_3$ system consistently displayed a smaller R_{ct} than the EY/Bi_2Se_3 system (specific values summarized in Table S5). This lower R_{ct} value for the $CoAs_3$ system indicates more rapid interfacial electron transfer kinetics compared to the Bi_2Se_3 system. This process includes both electron injection from the dye to the catalyst and the subsequent utilization of charge in the HER.

The interfacial charge transfer mechanism between photoexcited EY and the catalysts was investigated using in situ electron paramagnetic resonance (EPR) spectroscopy measured under illumination. In contrast to the weak intrinsic signal observed for pure EY under illumination, attributed to the formation of the excited state, the EY/catalyst mixtures exhibited a dramatic increase in signal intensity at $g = 2.001$ upon illumination (Fig. S15). This prominent *g*-value is characteristic of an organic radical, consistent with the formation of the EY radical cation (EY^+). Quantitatively, the EPR signal intensity for the EY/Bi_2Se_3 and EY/$CoAs_3$ mixtures was enhanced by factors of 6.1 and 26, respectively, relative to that of pure EY under the same illumination. This signal enhancement provides the spectroscopic evidence for efficient electron transfer from photoexcited EY to the catalyst, leading to the generation of the EY^+ radical cation. The larger signal enhancement factor for $CoAs_3$ (26) compared to that for Bi_2Se_3 (6.1) indicates that $CoAs_3$ more readily accepts an electron from photoexcited EY, leading to more effective charge separation.

Femtosecond TA spectroscopy was used to investigate the ultrafast charge transfer dynamics between the EY photosensitizer and the prepared catalysts with an excitation wavelength of 570 nm. By systematically investigating the ultrafast carrier dynamic processes of pure EY solution and the EY/Cat composites, we have obtained direct spectroscopic evidence of photoinduced electron transfer (PET) and resolved the subsequent multi-step kinetic pathways. The two-dimensional pseudo-color maps for pristine EY/$CoAs_3$ and EY composite are presented in Fig. 3a, d, respectively, with the data for EY/Bi_2Se_3 provided in the Supporting Information (Fig. S7a).

To establish a benchmark, the transient behavior of pristine EY was characterized to understand its intrinsic photophysical processes. The TA spectrum of pristine EY (Fig. 3e) exhibits a positive photoinduced absorption (PIA) band centered at 420 nm and a negative bleach signal centered at 510 nm. According to the previous report, the PIA signal is assigned to the absorption of singlet *EY, while the bleach signal comprises the broad ground-state bleach and stimulated emission of EY[61,62]. In stark contrast, the introduction of the catalysts in EY/Cat composites leads to an obvious change in their TA spectra. Besides the PIA band centered at 420 nm (for *EY) and the negative bleach signal at 510 nm present in pure EY, both the TA spectra of EY/$CoAs_3$ and EY/Bi_2Se_3 (Figs. 3b and S7a) still show an additional PIA signal with its peak at 470 nm, which is the definitive signature of the EY radical cation (EY^+). This emergence of EY^+ provides direct spectroscopic evidence for electron transfer from the excited EY to the catalyst, which can also be clearly reflected in their respective TA kinetics.

In pristine EY, the similar TA kinetics probed, respectively, at 420 and 445 nm are observed (Fig. 3f), while in EY/Cat composites, their TA kinetics probed at 420 and 470 nm exhibit completely different behaviors. The PIA signal at 420 nm shows a fast decay in the initial 2 ps delay, accompanied by a clear rising process of PIA signal at 470 nm in the same time scale (Figs. 3c and S7c), again verifying the PET from EY to the catalyst. Fig. 3g compares the PIA kinetics probed at 420 nm in pure EY and the EY/Cat composites. Compared with pure EY, both the excited states in the two EY/Cat composites exhibit evidently faster decay kinetics, which can be well fitted by a tri-exponential function (Table 1). Obviously, the fastest process (with $\tau_1 = 2.1$ ps and 3.2 ps for EY/$CoAs_3$ and EY/Bi_2Se_3, respectively) is attributable to the PET process, also consistent with the rise time observed in the PIA kinetics at 470 nm, while the slowest time constant exactly represents the lifetime of the charge-separated state. We also note that the faster process with time constant (τ_2) about tens of ps, likely originates from the accelerated decay of EY excited states in EY/Cat composites[61]. The above kinetics comparison between EY/$CoAs_3$ and EY/Bi_2Se_3 suggests the faster PET rate and longer lifetime of charge-separated state at the EY/

https://doi.org/10.1038/s41467-025-63843-y

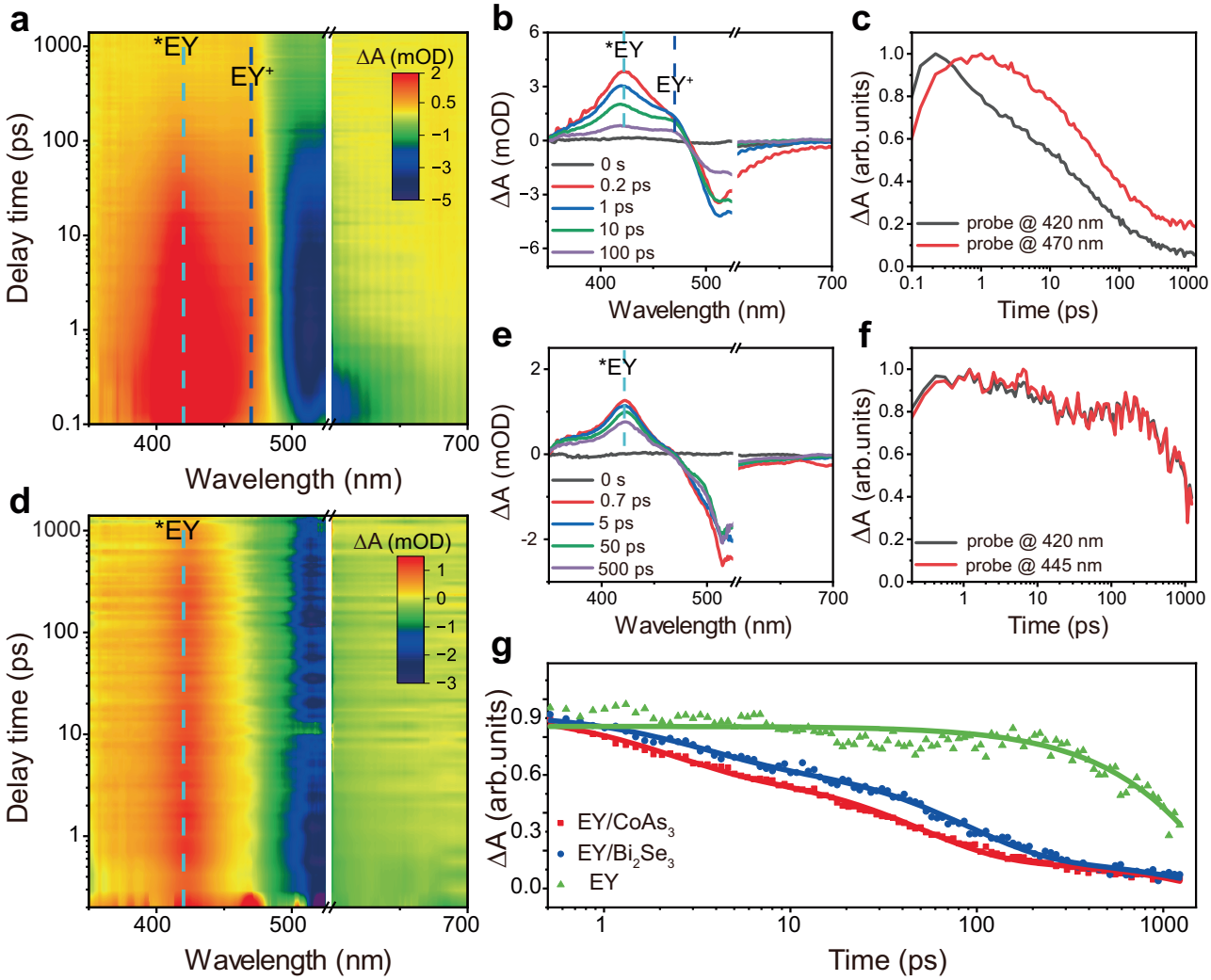

Fig. 3 | Ultrafast carrier dynamics at the EY/catalyst interface. Time slices of the TA spectra of **a**, **b** EY/$CoAs_3$ composite and **d**, **e** pure EY solution under excitation at 570 nm. Comparison of the TA kinetic probed at different wavelengths in EY/$CoAs_3$ (**c**) and EY (**f**). **g** Comparison of the TA kinetic probed at 420 nm between in EY solution (green), EY/$CoAs_3$ (red), and EY/Bi_2Se_3 (blue). Solid lines are their tri-exponential decay fitting. Source data for Fig. 3 are provided as a Source data file.

Table 1 | Summary of kinetic parameters obtained from multi-exponential fitting of the transient absorption decays at 420 nm

	A1 (%)	T1 (ps)	A2 (%)	T2 (ps)	A3 (%)	T3 (ps)
EY/$CoAs_3$	28.0	2.13	41.2	49.67	30.8	3245.22
EY/Bi_2Se_3	24.5	3.24	46.9	86.12	28.6	2989.68
EY	>>1.5ns					

$CoAs_3$ interface over the Bi_2Se_3 interface, which can account for the higher photocatalytic hydrogen production activity of the $CoAs_3$ catalyst.

DFT-calculated electronic structure of $CoAs_3$

Following electron transfer from the excited photosensitizer, the subsequent transport of electrons to surface active sites is governed by the electronic structure of the catalyst material. We therefore investigate the electronic structure of $CoAs_3$ by DFT calculations and compare it with that of other photocatalysts investigated in the current work.

The concept of topological catalysis has recently attracted considerable interest[38,63–67]. In contrast to TIs, the bulk states of topological semimetals are conductive. This conductivity, along with elevated electronic mobility, is thought to be beneficial for catalytic processes[37,38]. In addition, topological semimetals are found to carry a large number of topological emergent characters, including different categories of nodal points, nodal lines, and nodal surfaces[65,68,69]. These topological emergent characters also show diverse surface states. Consequently, both theoretical and experimental studies have identified topological semimetals as promising catalysts. Their proposed catalytic advantages are attributed to a combination of properties, including bulk-state conductivity, topologically protected surface states, and favorable molecular adsorption energies[6,41,70–79]. However, the mechanism responsible for the photocatalytic activity of $CoAs_3$ remains unclear, and the specific material properties that determine its performance in the HER have yet to be identified.

DFT calculations were performed to investigate the band structure of $CoAs_3$ (Fig. 4a), which provides insight into its photocatalytic behavior. The relaxed crystalline structure of $CoAs_3$ is provided as Supplementary Dataset 1. Without considering the spin–orbit coupling (SOC) effect, a threefold band crossing node appears at the high-symmetric Γ point, characterized by a topological charge $c = 0$ (Fig. 4b). Upon incorporating SOC, this threefold degeneracy evolves into a sixfold band crossing node. This node further splits into a

https://doi.org/10.1038/s41467-025-63843-y

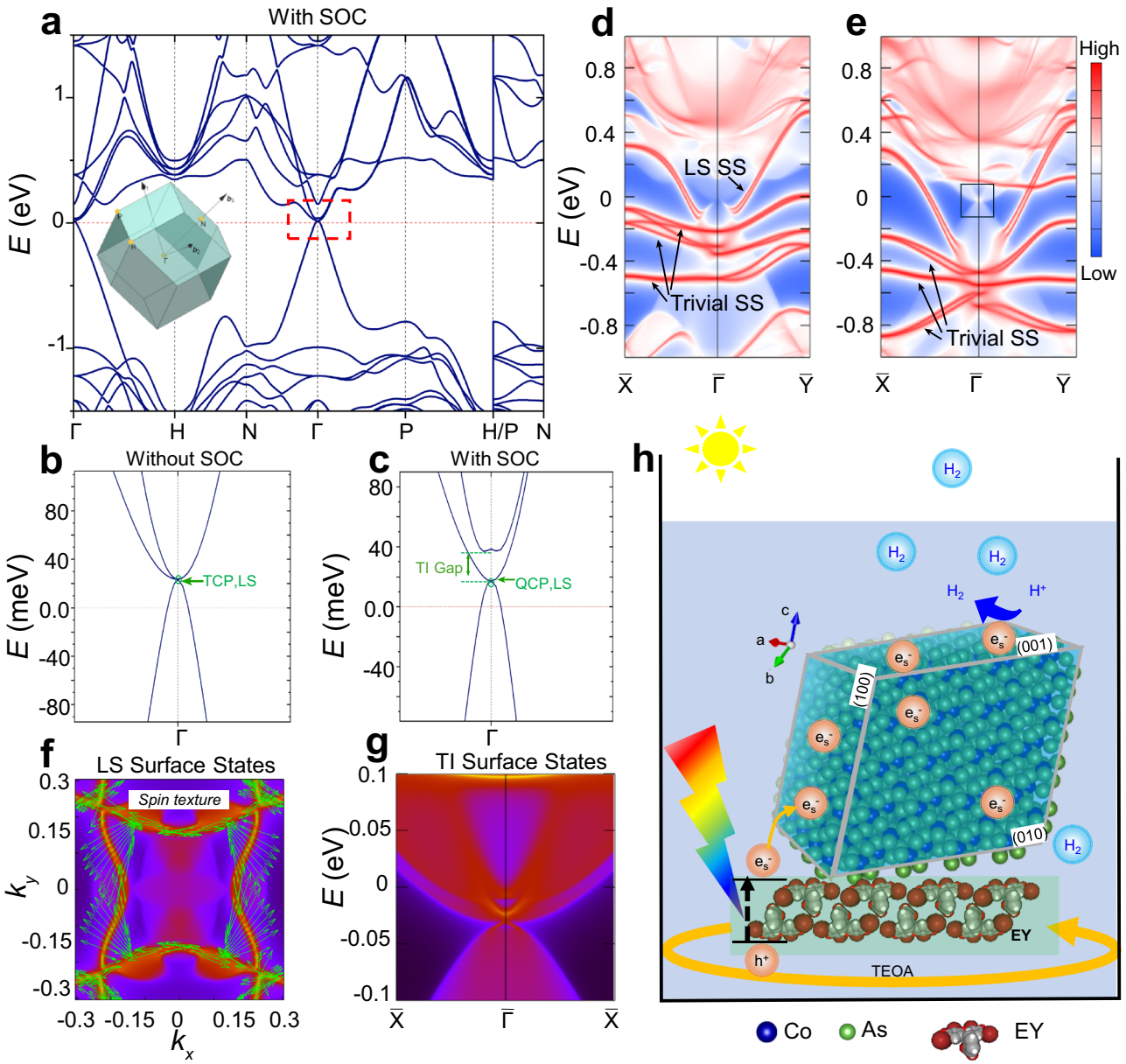

Fig. 4 | The calculated band structure and surface states of $CoAs_3$, and the proposed mechanism of enhanced photocatalytic HER performance. **a** Electronic band structure of $CoAs_3$ considering the SOC. Insert: bulk Brillouin zones of $CoAs_3$. **b**, **c** The enlarged view of the dashed red area for the enlarged band crossing points with and without SOC along the high symmetry path N–Γ–P in (**a**). The quadratic contact point at Γ above E_F. (TCP triple contact-point, QCP quadratic contact-point, LS Luttinger semimetal). **d**, **e** Surface band structures of the top and down surfaces. Note, the trivial surface states are induced by unsaturated dangling bonds on the surface, where the surface states of Luttinger semimetal are clearly shown. **f** Color mapping of the calculated spin texture of Luttinger semimetal (LS) surface states. **g** Color plot of the calculated topological insulator (TI) surface states. **h** The proposed mechanism of enhanced visible light photocatalytic HER performance of $CoAs_3$. Source data for Fig. 4 are provided as a Source data file.

twofold band crossing (triple contact-point (TCP)) and a fourfold degenerate quadratic contact-point (QCP), a phenomenon attributed to the coexistence of center-reversal symmetry and time-reversal symmetry. The presence of these degenerate points is indicative of the electronic structure of $CoAs_3$, potentially offering high carrier mobility and efficient electron pathways as well as efficient charge separation and transport in photocatalytic hydrogen evolution. In between the TCP and QCP, there is a TI gap and a Dirac-like topological surface state (Fig. 4c). The QCP along with specific surface states constitute a Luttinger semimetal (LSM)[80–82], where this degeneracy appears as a quadratic band touching of $j = 3/2$ fermions. LSMs have been studied due to their proximity to Z2 TIs[83], Dirac[84], and Weyl semimetals[85]. This nodal point is formed by the crossing of the valence band maximum and two conduction bands near the conduction band minimum and is protected by time-reversal symmetry and spatial-inversion symmetry. Detailed band structure analysis (Fig. 4b) indicates that the fourfold band degeneracy at the Γ point, near the Fermi level, primarily originates from the Co *d*-orbitals. Concurrently, with the inclusion of SOC, the sixfold nodal point transforms into a fourfold degenerate quadratic Dirac point (Fig. 4c)[84]. To further investigate the nontrivial band topology of $CoAs_3$, its surface band structure was calculated (Fig. 4d, e). These calculations show both Luttinger surface states (LSS) crossing the E_F and the concomitant appearance of trivial surface states. The presence of these conductive surface states, particularly those crossing E_F, can serve as efficient channels for transferring photogenerated electrons to the surface active sites, thereby reducing charge

recombination and enhancing hydrogen evolution efficiency. Further calculations reveal the spin texture of the LSS (Fig. 4f), exhibiting a characteristic spin-momentum locked pattern. This spin-momentum locked pattern can suppress backscattering of electrons, thereby reducing recombination, a process beneficial for photocatalysis. A magnified view of the region near the Γ point at the Fermi level (E_F) shows that the TI surface states become apparent (Fig. 4g). Since both the LSS and the TI surface states are protected by chiral symmetry and time-reversal symmetry, respectively, they are insensitive to disorder or impurities that do not break these specific symmetries. This property helps to ensure that efficient and stable charge carrier transport channels persist even in imperfect or complex catalytic environments, thereby contributing to sustained activity and high overall efficiency. The surface states emanated from the bulk nodal points of CoP_3 have been observed by angle-resolved photoemission spectroscopy measurements[86] and are seen to cross through E_F. Compared to Bi_2Se_3, $CoAs_3$ possesses both a fourfold degenerate quadratic Dirac point near E_F and the LSS crossing the E_F. These features contribute to a higher carrier density and high mobility in $CoAs_3$, whereas Bi_2Se_3 has only conventional topological surface states crossing E_F. The band structure calculations (Figs. 4 and S8) indicate that the *d*-orbitals of Co are the primary contributors to the electronic states near the E_F, leading to the formation of a topological Dirac cone. These topological features could enhance the efficiency of catalytic reactions such as the photocatalytic HER.

The intrinsic nature of high dye-sensitized activity of HER using $CoAs_3$ catalyst can be rationally explained in Fig. 4h. Upon light absorption, the EY photosensitizer generates an electron–hole pair. The electron is injected into the $CoAs_3$ catalyst, leaving a hole on the EY molecule. The conductive topological surface states of $CoAs_3$ facilitate the transport of these injected electrons away from the interface, thus suppressing charge recombination. This process contrasts with that in conventional semiconductors, where charge carriers are often annihilated by defects. In $CoAs_3$, the topological surface states allow electrons to bypass such defects, which helps to preserve the population of photo-generated electrons. Then, the surviving surface electrons are captured by protons adsorbed on the surface and generate H_2. Furthermore, the Co *d*-band crosses the E_F (Supplementary Fig. S7). These states are closely related to hydrogen interaction and are proposed to act as the active sites for HER. Meanwhile, the sacrificial electron donor (TEOA) contributes electrons to the photosensitizer and maintains the surface redox reactions.

In summary, this work introduces the topological LSM $CoAs_3$ as a catalyst for dye-sensitized photocatalytic hydrogen evolution. A comparison with other topological materials was performed to evaluate its performance. Under visible light ($\lambda \geq 420$ nm), the $CoAs_3$-based DSP system achieved a hydrogen production rate of 2688 μmol $h^{-1}g^{-1}$. Ultrafast spectroscopy confirmed rapid electron transfer at the EY/$CoAs_3$ interface, and theoretical calculations pointed to the role of the material's topological semimetal nature in its photocatalytic activity. This work identifies a topological semimetal as a stable and active catalyst for photocatalytic HER under visible light. The activity of the system under broad-spectrum illumination suggests a potential for hydrogen production using natural sunlight.

Methods

Reagents

Cobalt (Sigma Aldrich, 99.99%), Arsenic (Sigma Aldrich, 99.99%), Tungsten (Alfa Aesar, 99.95%), Tellurium (Alfa Aesar, 99.999%), molybdenum (Alfa Aesar, 99.95%), carbon (Alfa Aesar, 99.9%), Bismuth selenide (Sigma Aldrich, 99.99%) Bismuth(III) telluride (Sigma Aldrich, 99.99%), Eosin Y (Sigma Aldrich, 99%), TEOA (ACROS organics, 99+%), TiO_2 (Degussa P25).

Sample preparation

$CoAs_3$: The sample were prepared via solid-phase reaction. Co and As were sealed in quartz tubes in a stoichiometric ratio, heated to 800 °C at a rate of 100 °C per hour, held for 48 h, and cooled down with the furnace.

WTe_2: W and Te were ground stoichiometrically in an argon-filled glove box and sealed in an ampoule under vacuum, heated to 700 °C for 7 h and held for 1 day, then heated to 750 °C for 1 h and held for a period of time before being cooled in the furnace.

Mo_2C: Carbon and molybdenum were mixed and ground in stoichiometric ratio in an argon-filled glove box and pressed into tablets, flame sealed in ampoules under vacuum and cooled with the furnace after 10 h of heating to 950 °C.

HfP_2: The ingredients were combined and ground in stoichiometric proportions in an argon-filled glove box, then compressed into tablets. These were subsequently sealed under vacuum in ampoules and cooled with the furnace after 8 h of heating to 750 °C.

Characterization

The element distribution and the chemical composition of the products were determined through EDS mapping and spot analysis (Hitachi S-4800 scanning electron microscope) and TEM (HITACHI HF 5000), respectively. The chemical composition and crystal lattice structure were determined by XRD (Bruker-D8) with CuKα radiation over an angular range of 10–90° in 1 h at room temperature. The chemical valence states were detected using an XPS (Kratos AXIS ULTRA XPS).

DSP HER

The photocatalytic reactions occurring in hydrogen were carried out in a sealed gas–solid atmospheric pressure cylindrical glass reactor. The light source was a 300 W xenon lamp with a 420 nm cut-off filter. In all, 100 mg of catalyst powder was dispersed in 100 ml of freshly prepared aqueous TEOA (15%v/v), and 0.014 mmol (9.07 mg) of EY was added to the glass reactor, followed by sonication for 30 min to ensure homogeneous particle dispersion (ph = 10.15 ± 0.1). The vessel was positioned upon a magnetic stirrer, and the vacuum pump was activated to commence the photocatalytic process. This was followed by the illumination and agitation of the sample to initiate the reaction.

Apparent quantum efficiency

The AQE can be described based on the following formula:

$$AQE\,(\%) = ARN_A/I \times 100$$

where *A, R, N_A*, and *I* represent a coefficient (2 for H_2 evolution), the evolution rate of H_2, Avogadro's constant, and the number of photons absorbed by the reaction solution, respectively. For evaluating the AQE, the reactions were performed under similar reaction conditions except that the monochromatic light was used. As the light source, the monochromatic light was generated by Xe lamp equipped with the band-pass filters centered at 380, 420, 450, 500, 550, and 600 nm, respectively.

TA spectroscopy

The femtosecond pump-probe TA measurements were performed using a regenerative amplified Ti:sapphire laser system (Coherent; 800 nm, 70 fs, 6 mJ $pulse^{-1}$, and 1 kHz repetition rate) as the laser source and a femto-TA100 spectrometer (Time-Tech Spectra). All experiments were performed under ambient conditions.

First-principles calculations

First-principles calculations were performed based on DFT by utilizing the Vienna ab initio simulation package[87,88]. The plane-wave basis was adopted with an energy cutoff of 350 eV. The electron–ion interactions

were modeled with the projector augmented wave potential[89], and the exchange–correlation functional was approximated by the Perdew–Burke–Ernzerhof-type generalized gradient approximation[90]. For optimized lattice constants and atomic positions, the structural relaxation was performed with an energy (force) criterion of 10^{-8} eV (0.01 eV $Å^{-1}$) and by utilizing the DFT-D3[91] method to include van der Waals corrections. Surface state calculations were performed with the Wannier Tools package[92], which is based on the tight-binding Hamiltonians constructed from maximally localized Wannier functions[93].

Data availability

All data generated or analyzed during this study are included in this published article and its Supplementary Information files. Source data are provided with this paper.

References

1. Lewis, N. S. & Nocera, D. G. Powering the planet: chemical challenges in solar energy utilization. *Proc. Natl. Acad. Sci. USA* **103**, 15729–15735 (2006).
2. Wang, Z., Goddard, W. A. 3rd & Xiao, H. Potential-dependent transition of reaction mechanisms for oxygen evolution on layered double hydroxides. *Nat. Commun.* **14**, 4228 (2023).
3. Abdullah, H. et al. Variation of Ni and Mg dopants in spinel $ZnIn_2(O,S)_4$ microflower to generate NiIn– and MgIn– substitutional defects for a high-rate visible-light-induced hydrogen generation. *J. Environ. Chem. Eng.* **11**, 110500 (2023).
4. Bie, C., Wang, L. & Yu, J. Challenges for photocatalytic overall water splitting. *Chem* **8**, 1567–1574 (2022).
5. Fan, Y., Wang, J. & Zhao, M. Spontaneous full photocatalytic water splitting on 2D $MoSe_2/SnSe_2$ and $WSe_2/SnSe_2$ vdW heterostructures. *Nanoscale* **11**, 14836–14843 (2019).
6. Lin, Z. et al. A floating sheet for efficient photocatalytic water splitting. *Adv. Energy Mater.* **6**, 1600510 (2016).
7. Min, S. & Lu, G. Enhanced electron transfer from the excited eosin Y to mpg-C_3N_4 for highly efficient hydrogen evolution under 550 nm irradiation. *J. Phys. Chem. C* **116**, 19644–19652 (2012).
8. Herbrik, F. et al. Eosin Y: homogeneous photocatalytic in-flow reactions and solid-supported catalysts for in-batch synthetic transformations. *Appl. Sci.* **10**, 5596 (2020).
9. Yan, Z. et al. Enhanced visible light-driven hydrogen production from water by a noble-metal-free system containing organic dye-sensitized titanium dioxide loaded with nickel hydroxide as the cocatalyst. *Appl. Catal. B Environ.* **160**, 173–178 (2014).
10. O'regan, B. & Grätzel, M. A low-cost, high-efficiency solar cell based on dye-sensitized colloidal TiO_2 films. *Nature* **353**, 737–740 (1991).
11. Lewandowska-Andrałojć, A. et al. How Eosin Y/graphene oxide-based materials can improve efficiency of light-driven hydrogen generation: mechanistic aspects. *J. Phys. Chem. C* **124**, 2747–2755 (2020).
12. Lynch, P. G., Richards, H. & Wustholz, K. L. Unraveling the excited-state dynamics of eosin Y photosensitizers using single-molecule spectroscopy. *J. Phys. Chem. A* **123**, 2592–2600 (2019).
13. Kopera, K. M. et al. Origin of kinetic dispersion in eosin-sensitized TiO_2: insights from single-molecule spectroscopy. *J. Phys. Chem. C***125**, 23634–23645 (2021).
14. Pastor, E. et al. Spectroelectrochemical analysis of the mechanism of (photo) electrochemical hydrogen evolution at a catalytic interface. *Nat. Commun.* **8**, 14280 (2017).
15. Reynal, A. et al. Parameters affecting electron transfer dynamics from semiconductors to molecular catalysts for the photochemical reduction of protons. *Energy Environ. Sci.* **6**, 3291–3300 (2013).
16. Kobayashi, D. et al. Significant enhancement of hydrogen evolution reaction activity by negatively charged Pt through light doping of W. *J. Am. Chem. Soc.* **142**, 17250–17254 (2020).
17. Kuang, P. et al. Pt single atoms supported on N-doped mesoporous hollow carbon spheres with enhanced electrocatalytic H_2-evolution activity. *Adv. Mater.* **33**, 2008599 (2021).
18. Liang, L. et al. Cobalt single atom site isolated Pt nanoparticles for efficient ORR and HER in acid media. *Nano Energy* **88**, 106221 (2021).
19. McCrum, I. T. & Koper, M. arcT. M. The role of adsorbed hydroxide in hydrogen evolution reaction kinetics on modified platinum. *Nat. Energy* **5**, 891–899 (2020).
20. Ye, S. et al. Highly stable single Pt atomic sites anchored on aniline-stacked graphene for hydrogen evolution reaction. *Energy Environ. Sci.* **12**, 1000–1007 (2019).
21. Jiang, H. et al. Ternary interfacial superstructure enabling extraordinary hydrogen evolution electrocatalysis. *Mater. Today* **21**, 602–610 (2018).
22. Poerwoprajitno, A. R. et al. Synthesis of low-and high-index faceted metal (Pt, Pd, Ru, Ir, Rh) nanoparticles for improved activity and stability in electrocatalysis. *Nanoscale* **11**, 18995–19011 (2019).
23. Qian, J. et al. Synthesis of Pt nanocrystals with different shapes using the same protocol to optimize their catalytic activity toward oxygen reduction. *Mater. Today* **21**, 834–844 (2018).
24. Seh, Z. W. et al. Combining theory and experiment in electrocatalysis: insights into materials design. *Science* **355**, eaad4998 (2017).
25. Zhuang, L. et al. Defect-induced Pt–Co–Se coordinated sites with highly asymmetrical electronic distribution for boosting oxygen-involving electrocatalysis. *Adv. Mater.* **31**, 1805581 (2019).
26. Khan, M. A. et al. Recent progresses in electrocatalysts for water electrolysis. *Electrochem. Energy Rev.* **1**, 483–530 (2018).
27. Nørskov, J. K. et al. Trends in the exchange current for hydrogen evolution. *J. Electrochem. Soc.* **152**, J23 (2005).
28. Wu, H. et al. Non-noble metal electrocatalysts for the hydrogen evolution reaction in water electrolysis. *Electrochem. Energy Rev.* **4**, 473–507 (2021).
29. Tiwari, A. P. et al. Layered ternary and quaternary transition metal chalcogenide based catalysts for water splitting. *Catalysts* **8**, 551 (2018).
30. Tiwari, A. P. et al. Continuous network of phase-tuned nickel sulfide nanostructures for electrocatalytic water splitting. *ACS Appl. Nano Mater.* **2**, 5061–5070 (2019).
31. Du, H. et al. Recent progress in transition metal phosphides with enhanced electrocatalysis for hydrogen evolution. *Nanoscale* **10**, 21617–21624 (2018).
32. Tiwari, A. P. et al. Conformally coated nickel phosphide on 3D, ordered nanoporous nickel for highly active and durable hydrogen evolution. *ACS Sustain. Chem. Eng.* **8**, 17116–17123 (2020).
33. Yoon, Y. et al. Precious-metal-free electrocatalysts for activation of hydrogen evolution with nonmetallic electron donor: chemical composition controllable phosphorous doped vanadium carbide MXene. *Adv. Funct. Mater.* **29**, 1903443 (2019).
34. Yoon, Y. et al. Enhanced electrocatalytic activity by chemical nitridation of two-dimensional titanium carbide MXene for hydrogen evolution. *J. Mater. Chem. A* **6**, 20869–20877 (2018).
35. Cao, B. et al. Mixed close-packed cobalt molybdenum nitrides as non-noble metal electrocatalysts for the hydrogen evolution reaction. *J. Am. Chem. Soc.* **135**, 19186–19192 (2013).
36. Liu, B. et al. Unconventional nickel nitride enriched with nitrogen vacancies as a high-efficiency electrocatalyst for hydrogen evolution. *Adv. Sci.* **5**, 1800406 (2018).
37. Yang, Q. et al. Topological catalysis in the language of chemistry. *Innov. Mater.* **1**, 100013 (2023).
38. Xie, R., Zhang, T., Weng, H. & Chai, G.-L. Progress, advantages, and challenges of topological material catalysts. *Small Sci.* **2**, 2100106 (2022).

39. Weng, H. et al. Quantum anomalous Hall effect and related topological electronic states. *Adv. Phys.* **64**, 227–282 (2015).
40. Wang, L. et al. Excellent catalytic performance toward the hydrogen evolution reaction in topological semimetals. *EcoMat* **5**, e12316 (2023).
41. Samanta, M. et al. The Weyl semimetals $MIrTe_4$ (M = Nb,Ta) as efficient catalysts for dye-sensitized hydrogen evolution. *Adv. Energy Mater.* **13**, 2300503 (2023).
42. Rajamathi, C. R. et al. Weyl semimetals as hydrogen evolution catalysts. *Adv. Mater.* **29**, 1606202 (2017).
43. Ackermann, J. & Wold, A. The preparation and characterization of the cobalt skutterudites CoP_3, $CoAs_3$ and $CoSb_3$. *J. Phys. Chem. solids* **38**, 1013–1016 (1977).
44. Khan, M. R., Bu, K. & Wang, J.-T. Six-or four-fold band degeneration in $CoAs_3$, $RhAs_3$ and $RhSb_3$ topological semimetals. *Phys. Chem. Chem. Phys.* **23**, 25944–25950 (2021).
45. Grosvenor, A. P. *X-ray Spectroscopic Studies of Intermetallic Compounds*. Doctoral thesis, University of Alberta (2008).
46. Zhou, M. et al. Iodide and sulfite synergistically accelerate the photo-reduction and recovery of As(V) and As(III) in sulfite/iodide/UV process: efficiency and mechanism. *Water Res.* **252**, 121210 (2024).
47. Plucinski, L. et al. Robust surface electronic properties of topological insulators: Bi_2Te_3 films grown by molecular beam epitaxy. *Appl. Phys. Lett.* **98**, 22 (2011).
48. Wang, X. et al. Fragility of surface states and robustness of topological order in Bi_2Se_3 against oxidation. *Phys. Rev. Lett.* **108**, 096404 (2012).
49. Yuan, Y.-J. et al. Role of two-dimensional nanointerfaces in enhancing the photocatalytic performance of 2D-2D MoS_2/CdS photocatalysts for H_2 production. *Chem. Eng. J.* **350**, 335–343 (2018).
50. Lazarides, T. et al. Making hydrogen from water using a homogeneous system without noble metals. *J. Am. Chem. Soc.* **131**, 9192–9194 (2009).
51. Liu, X. et al. Photosensitization of $SiW_{11}O_{398}$–-modified TiO_2 by Eosin Y for stable visible-light H_2 generation. *Int. J. Hydrog. Energy* **38**, 11709–11719 (2013).
52. Liu, W. et al. Eosin Y embedded Gd-MOF as a dual emission detection platform for dopamine. *Inorg. Chem. Commun.* **160**, 111916 (2024).
53. Jha, B. K., Chaule, S. & Jang, J.-H. Enhancing photocatalytic efficiency with hematite photoanodes: principles, properties, and strategies for surface, bulk, and interface charge transfer improvement. *Mater. Chem. Front.* **8**, 2197–2226 (2024).
54. Alvarez-Martin, A. et al. Photodegradation mechanisms and kinetics of Eosin-Y in oxic and anoxic conditions. *Dyes Pigments* **145**, 376–384 (2017).
55. Chong, R. et al. 2D Co-incorporated hydroxyapatite nanoarchitecture as a potential efficient oxygen evolution cocatalyst for boosting photoelectrochemical water splitting on Fe_2O_3 photoanode. *Appl. Catal. B Environ.* **250**, 224–233 (2019).
56. Liu, G. et al. A tantalum nitride photoanode modified with a hole-storage layer for highly stable solar water splitting. *Angew. Chem. Int. Ed.* **53**, 7295–7299 (2014).
57. Yun, X. et al. A ternary-structured NiCo-LDH/Ni/$BiVO_4$ photoanode with enhanced charge dynamics for photoelectrochemical water splitting. *Surf. Interfaces* **56**, 105444 (2024).
58. Tu, L.-H. et al. A signal-off photoelectrochemical aptasensor for ultrasensitive 17β-estradiol detection based on rose-like CdS@ C nanostructure and enzymatic amplification. *Microchim. Acta* **189**, 56 (2022).
59. Kanmani, S. S. et al. Comparison of Eosin yellowish dye–sensitized and CdS-sensitized TiO_2 nanomaterial–based solid-state solar cells. *J. Solid State Electrochem.* **24**, 2499–2509 (2020).
60. Li, Z. et al. Eosin Y covalently anchored on reduced graphene oxide as an efficient and recyclable photocatalyst for the aerobic oxidation of α-aryl halogen derivatives. *ACS Sustain. Chem. Eng.* **3**, 468–474 (2015).
61. Tipping, M. B. et al. Ultrafast photoinduced electron transfer between donor (Eosin-Y) and acceptor (naphthoquinone) in a supramolecular array based on a coordination cage host. *Chem. Eur. J.***31**, e202404647 (2025).
62. Li, S. et al. Interaction between triethanolamine and singlet or triplet excited state of xanthene dyes in aqueous solution. *Spectrochim. Acta A Mol. Biomol. Spectrosc.* **184**, 204–210 (2017).
63. Burkov, A. A. Topological semimetals. *Nat. Mater.* **15**, 1145–1148 (2016).
64. Ding, G. et al. Charge-two Weyl phonons with type-III dispersion. *Phys. Rev. B* **105**, 134303 (2022).
65. He, T. et al. Ideal fully spin-polarized type-II nodal line state in half-metals X_2YZ_4 (X = K, Cs, Rb, YCr, Cu, Z = Cl, F). *Mater. Today Phys.* **17**, 100360 (2021).
66. Meng, W. et al. Antiferromagnetism caused by excess electrons and multiple topological electronic states in the electride $Ba_4Al_5{\cdot}e^-$. *Phys. Rev. B* **104**, 195145 (2021).
67. Murakami, S. et al. Emergence of topological semimetals in gap closing in semiconductors without inversion symmetry. *Sci. Adv.* **3**, e1602680 (2017).
68. Fang, C. et al. Topological nodal line semimetals. *Chin. Phys. B* **25**, 117106 (2016).
69. Yan, B. & Claudia, F. Topological materials: Weyl semimetals. *Annu. Rev. Condens. Matter Phys.* **8**, 337–354 (2017).
70. Kong, X.-P. et al. Development of a Ni-doped VAl_3 topological semimetal with a significantly enhanced HER catalytic performance. *J. Phys. Chem. Lett.* **12**, 3740–3748 (2021).
71. Li, G. et al. Dirac nodal arc semimetal $PtSn_4$: an ideal platform for understanding surface properties and catalysis for hydrogen evolution. *Angew. Chem.* **131**, 13241–13246 (2019).
72. Li, G. et al. Surface states in bulk single crystal of topological semimetal $Co_3Sn_2S_2$ toward water oxidation. *Sci. Adv.* **5**, eaaw9867 (2019).
73. Li, G. et al. Obstructed surface states as the descriptor for predicting catalytic active sites in inorganic crystalline materials. *Adv. Mater.* **34**, 2201328 (2022).
74. Li, J. et al. Topological quantum catalyst: Dirac nodal line states and a potential electrocatalyst of hydrogen evolution in the TiSi family. *Sci. China Mater.* **61**, 23–29 (2018).
75. Liu, W. et al. Theoretical realization of hybrid Weyl state and associated high catalytic performance for hydrogen evolution in NiSi. *iScience* **25**, 103543 (2022).
76. Tang, M. et al. Edge-state-enhanced CO_2 electroreduction on topological nodal-line semimetal Cu_2Si nanoribbons. *J. Phys. Chem. C* **123**, 2837–2842 (2019).
77. Wang, L. et al. A topological quantum catalyst: the case of two-dimensional traversing nodal line states associated with high catalytic performance for the hydrogen evolution reaction. *J. Mater. Chem. A* **9**, 22453–22461 (2021).
78. Yang, Q. et al. Enhancement of basal plane electrocatalytic hydrogen evolution activity via joint utilization of trivial and non-trivial surface states. *Appl. Mater. Today* **22**, 100921 (2021).
79. Yang, Q. et al. Topological engineering of Pt-group-metal-based chiral crystals toward high-efficiency hydrogen evolution catalysts. *Adv. Mater.* **32**, 1908518 (2020).
80. Hu, L.-H. & Zhang, R.-X. Topological superconducting vortex from trivial electronic bands. *Nat. Commun.* **14**, 640 (2023).
81. Kondo, T. et al. Quadratic Fermi node in a 3D strongly correlated semimetal. *Nat. Commun.* **6**, 10042 (2015).
82. Moon, E.-G. et al. Non-Fermi-liquid and topological states with strong spin-orbit coupling. *Phys. Rev. Lett.* **111**, 206401 (2013).

83. Dai, X. et al. Helical edge and surface states in HgTe quantum wells and bulk insulators. *Phys. Rev. B* **77**, 125319 (2008).
84. Xu, C.-Z. et al. Elemental topological Dirac semimetal: α-Sn on InSb (111). *Phys. Rev. Lett.* **118**, 146402 (2017).
85. Cano, J. et al. Chiral anomaly factory: creating Weyl fermions with a magnetic field. *Phys. Rev. B* **95**, 161306 (2017).
86. Fan, C. et al. Extremely large magnetoresistance in an unfilled skutterudite quadratic contact point semimetal CoP_3. *Appl. Phys. Lett.* **122**, 253103 (2023).
87. Kresse, G. & Furthmüller, J. Efficient iterative schemes for ab initio total-energy calculations using a plane-wave basis set. *Phys. Rev. B* **54**, 11169 (1996).
88. Kresse, G. & Joubert, D. From ultrasoft pseudopotentials to the projector augmented-wave method. *Phys. Rev. B* **59**, 1758 (1999).
89. Blöchl, P. E. Projector augmented-wave method. *Phys. Rev. B* **50**, 17953 (1994).
90. Perdew, J. P., Burke, K. & Ernzerhof, M. Generalized gradient approximation made simple. *Phys. Rev. Lett.* **77**, 3865 (1996).
91. Grimme, S., Antony, J., Ehrlich, S. & Krieg, S. A consistent and accurate ab initio parametrization of density functional dispersion correction (DFT-D) for the 94 elements H-Pu. *J. Chem. Phys.* **132**, 154104 (2010).
92. Wu, Q., Zhang, S., Song, H.-F., Troyer, M. & Soluyanov, A. A. WannierTools: an open-source software package for novel topological materials. *Comput. Phys. Commun.* **224**, 405 (2018).
93. Mostofi, A. A. et al. An updated version of wannier90: a tool for obtaining maximally-localised Wannier functions. *Comput. Phys. Commun.* **185**, 2309 (2014).

Acknowledgements

Sample growth, TEM work, and photocatalytic HER was done at the School of Physics and Information Technology and School of Chemistry and Chemical Engineering, Shaanxi Normal University. This work is financially supported by the National Key R&D Program of China (Nos. 2022YFA1403100, 2022YFA1403101, and 2022YFA1403903), the National Natural Science Foundation of China (Nos. 22372096, 11574095, and 91745115) and the Chinese Academy of Sciences (XDB0970000 and YSBR-07).

Author contributions

Y. Ma and M. Pan conceived and designed the experiments. J. Gao, C. Wang, Y. Yu, F. Song, and W. Huang helped to locate the research resource related to this work. Y. Cao, X. Tian, Y. Liu, and Z. Han performed HER measurements. Y. Cao, S. Xia, X. Tian, X. Zhang, J. Leng, and C. Zhou performed absorption and photoluminescence (PL) spectra measurement. Y. Cao, J. He, Y. Zou, and W. Zhu grew the samples. R. Song carried out the DFT calculations. Y. Ma and M. Pan analyzed the data. M. Pan, C. Zhou, and Y. Ma wrote the manuscript with inputs from all other authors.

Competing interests

The authors declare no competing interests.

Additional information

Supplementary information The online version contains supplementary material available at https://doi.org/10.1038/s41467-025-63843-y.

Correspondence and requests for materials should be addressed to Wenliang Zhu, Yi Ma, Jianzhi Gao, Chuanyao Zhou, Feng Song, Wei Huang or Minghu Pan.

Peer review information *Nature Communications* thanks Youyong Li and the other anonymous reviewer(s) for their contribution to the peer review of this work. A peer review file is available.